Numerical simulations of the natural convection in a cavity with nonuniform internal sources

M. J. Coates and J. C. Patterson

Department of Environmental Engineering and Centre for Water Research, University of Western Australia, Nedlands, Western Australia

A numerical code based on the SIMPLE algorithm and defined on a nonstaggered grid was used to simulate the natural convection in a cavity heated by the nonuniform absorption of radiation entering through part of the surface. After the code was validated against laboratory experiments, it was used to extend the results over a larger range of radiation parameters than were available in the laboratory. The extended results were used to derive empirical relations that could be used to predict the intrusion velocities and time scales in small lakes.

1. Introduction

Local concentrations of suspended particulate matter on the surface of lakes and reservoirs give rise to a reduction in the penetration of solar radiation through the surface. The particulate matter may be of either animate (for example, photoplankton) or inanimate (for example, detrital material) origin, but in both cases the material is usually dark, and the particles cause an increase in the path length of the incoming radiation, effectively preventing the solar radiation from penetrating beyond the depth of the turbid patch. The absorption of solar radiation in turbid waters can be up to two orders of magnitude greater than in clear waters (Kirk 1986).

The presence of floating vegetation mats (Bowmaker 1976) or hyperscums (Zohary and Madeira 1990), for example, gives rise to a similar effect, in that the solar radiation is prevented from entering the body of the water column. In both cases, the region beneath the patch is shielded from radiation, whereas the regions beyond the extent of the patch are not and are consequently heated at a higher rate. The result is a relatively cool region beneath the patch, with a corresponding horizontal pressure gradient. The resulting flow from the open to the shaded region may be of considerable significance biologically, in that the supply of nutrients to a biologically active patch may be provided by this flow. Thus the rate of supply may be limited in some sense by the development of this flow, and a natural limitation on the patch size may occur. In any case, the relative time scales of transport and uptake of nutrients are of some interest to limnologists.

This mechanism of horizontal transport in lakes was discussed by Patterson and Imberger (1990), and a scaling, numerical, and experimental analysis of the mechanism was described by Coates and Patterson (1993), hereinafter referred to as CP. Their work extended the analyses of Patterson (1984) and Trevisan and Bejan (1986), both of which dealt with the

natural convection flows driven by horizontally varying internal heat sources. The latter paper in particular considered the case of a horizontally infinite region in which the distribution of sources was such that the differential absorption of radiation was modeled by two regions, each with constant but different source intensities and each of different depths. In CP, the constant source was replaced by one in which the intensity varied in a decaying exponential manner with depth, modeling the attenuation of radiation intensity with increasing depth. This introduced an additional length scale into the model, of which the Trevisan and Bejan model was a special case.

The specific problem examined by CP was that of a cavity in which one half of the surface was opaque to incoming radiation, while the remainder of the surface was transparent, allowing the water beneath to be heated by absorption of the radiation. The water was initially stationary and isothermal. The radiation source was instantaneously increased to and maintained at a fixed value. An analysis of the relationship between the time, length, and velocity scales showed that a number of transient flow regimes were possible, depending on the relationship between the various parameters of the problem. However, it was also shown that virtually all naturally occurring problems fell into one regime for which $\mathrm{Gr} > \eta^4 h^4 \mathrm{Pr}^{-3}$, where the Grashof number Gr and the Prandtl number Pr are defined, respectively, by

$$\mathrm{Gr} = \frac{g \alpha F_0 h^4}{\rho_0 C_\mathrm{p} \nu^3} \tag{1}$$

and

$$\mathrm{Pr} = \frac{\nu}{\kappa} \tag{2}$$

and α is the coefficient of thermal expansion, ν the kinematic viscosity, κ the thermal diffusivity, ρ_0 the reference density, and C_p the specific heat at constant pressure of the water. The depth of the cavity is h and the gravitational acceleration is g, while the total intensity of radiation at depth z is given by Beer's Law:

$$F(z) = F_0 \exp[-\eta_\mathrm{b} z] \tag{3}$$

where F_0 is the bulk or effective radiation intensity at the surface (in $Jm^{-2}sec^{-1}$), while η_b is the bulk or effective attenuation coefficient (in m^{-1}). Equation 3 may be written more accurately as

$$F(z) = \sum_{i=1}^{N} F_i^0 \exp[-\eta_i z] \tag{4}$$

where the N discrete wavelength bands are characterized by surface intensities F_i^0 and attenuation coefficients η_i.

In this regime, the initial stage of the flow was an intrusion traveling from the heated to the shaded part of the cavity beneath the radiation-blocking region. According to the CP scaling analysis, the intrusion was characterized by a sequence of velocity and time scales as the flow developed and the various balances changed. In particular in this regime, the intrusion flow was initially characterized by a balance between the unsteady term and the buoyancy-induced pressure gradient, but after a time scale of order

$$t_c \sim \left(\frac{\kappa h^4}{Grv^3}\right)^{1/2} \tag{5}$$

there was a switch to a balance between inertia and buoyancy, with a velocity scale given by

$$u_I \sim \left(\frac{Grv^3 t}{h^4}\right)^{1/2} \tag{6}$$

The balance changed again at time t_E, when the transport of heat away by the intrusion balanced the input of heat through the surface, with a resulting so-called energy limited velocity scale of

$$u_E \sim \left(\frac{Grv^3 l_E}{h^4}\right)^{1/3} \tag{7}$$

where l_E is the length of the exposed surface, and the time scale

t_E is given by

$$t_E \sim \left(\frac{h^4 l_E^2}{Grv^3}\right)^{1/3} \tag{8}$$

CP undertook an extensive experimental and more limited numerical verification of the scaling, and to a large degree confirmed these and other results obtained for this regime.

The results of CP were limited, however, by the relatively small range of radiation parameters available in the laboratory, and the O(1) constants in some of the scaling relationships were not conclusively obtained. In this paper, a series of numerical experiments is described that extends the parameter range and allows the coefficients relating the radiation parameters to the flow characteristics to be better defined. These coefficients then allow estimates to be made of the net horizontal transport under a floating patch in a lake or reservoir.

2. Numerical scheme

Under consideration is a rectangular cavity of height h and length $(l + l_E)$, where l is the shaded length. All the boundaries are nonslip and rigid. While it is appreciated that in real situations with floating plant layers, the upper surface is a free surface, experiments by Coates and Ferris (1994) showed that this boundary type is relatively unimportant. However, since a nonslip boundary was used in the experiments of CP, we choose to retain it in the simulations that follow. The thermal boundary conditions are that the end walls are held at temperature T_0 and that the upper and lower boundaries are assumed insulated. This latter assumption is equivalent to saying that the surface heat transfers by conduction and by long-wave radiation are small compared with the absorption of solar radiation, and that all heat input to the cavity through the surface is by the absorption of the solar radiation. Initially, the fluid is stationary and at temperature T_0 (see Figure 1). At time $t = 0$, the total surface radiation is instantaneously

---

Notation

*	Indicates a dimensioned parameter in the nondimensional scheme
A	Aspect ratio h/l (shaded region)
A_E	Aspect ratio h/l_E (illuminated region)
D	Intrusion thickness
d	Nondimensionalized intrusion thickness
$F(z)$	Total intensity of radiation at depth z
F_i^0	Radiation intensity at the surface within waveband i
F_0	Bulk or effective radiation intensity at the surface
C_P	Specific heat at constant pressure
g	Gravitational acceleration
Gr	Grashof number
$H(x)$	"Illumination" step function
h	Depth of the cavity
i	Summation index
l	Length of shaded region; nondimensionalized length of travel
l_E	Length of illuminated regime
N	Number of wavebands
Pr	Prandtl number
p	Pressure (relative to hydrostatic)
r_x	Horizontal grid expansion factor
r_z	Vertical grid expansion factor
T	Temperature

T_0	Initial temperature
t	Time
t_c	Time to the inertia-buoyancy balance
t_E	Time to the energy-limited regime
t_e	Measured time to the energy-limited regime
u	Horizontal velocity
$\overline{u_E}$	Energy-limited velocity scale
$\overline{u_e}$	Measured energy-limited velocity scale
u_I	Inertial velocity scale
V	Volume
W	Intrusion width
w	Vertical velocity
x	Horizontal axis
z	Vertical axis

Greek symbols

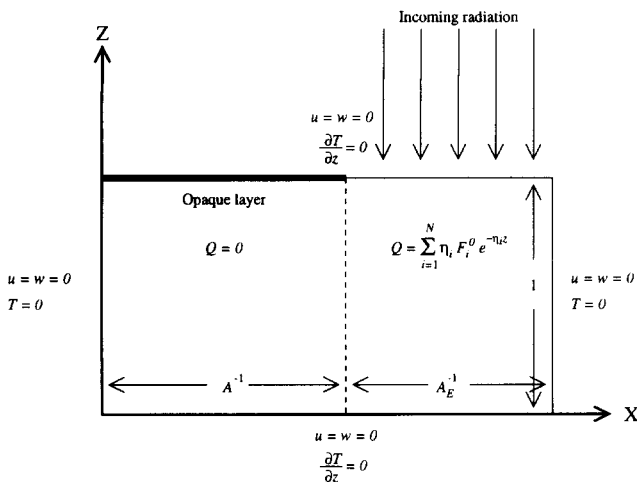|	
α	Coefficient of thermal expansion
Δx_1	Initial horizontal grid size
Δz_1	Initial vertical grid size
η_i	Attenuation coefficient within waveband i
η_b	Bulk or effective attenuation coefficient
κ	Thermal diffusivity
v	Kinematic viscosity
ρ_0	Reference density

Figure 1 A sketch of the cavity with its dimensionless boundary conditions. The initial conditions are $u = w = 0$ and $T = 0$ everywhere

increased from zero to its working value and maintained at that value thereafter.

The equations that describe the subsequent motion are the usual Boussinesq equations, written in nondimensional form as

$$\frac{\partial u}{\partial x} + \frac{\partial w}{\partial z} = 0 \tag{9}$$

$$\frac{\partial u}{\partial t} + A_E\left(u\frac{\partial u}{\partial x} + w\frac{\partial u}{\partial z}\right) = -\frac{\partial p}{\partial x} + \left(\frac{A_E^2}{Gr}\right)^{1/3}\left(\frac{\partial^2 u}{\partial x^2} + \frac{\partial^2 u}{\partial z^2}\right) \tag{10}$$

$$\frac{\partial w}{\partial t} + A_E\left(u\frac{\partial w}{\partial x} + w\frac{\partial w}{\partial z}\right) = -\frac{\partial p}{\partial z} + \left(\frac{A_E^2}{Gr}\right)^{1/3}\left(\frac{\partial^2 w}{\partial x^2} + \frac{\partial^2 w}{\partial z^2}\right) + A_E T \tag{11}$$

and

$$\frac{\partial T}{\partial t} + A_E\left(u\frac{\partial T}{\partial x} + w\frac{\partial T}{\partial z}\right) = \frac{1}{Pr}\left(\frac{A_E^2}{Gr}\right)^{1/3}\left(\frac{\partial^2 T}{\partial x^2} + \frac{\partial^2 T}{\partial z^2}\right)$$
$$+ H(x)\sum_{i=1}^{N} \eta_i F_i^0 \exp[-\eta_i z] \tag{12}$$

where the aspect ratio based on the exposed length is $A_E = h/l_E$.

The function $H(x)$ defines the shaded and unshaded regions of the surface, so that

$$H(x) = \begin{cases} 0 & \text{for } 0 \le x < A^{-1} \\ 1 & \text{for } A^{-1} \le x \le (A^{-1} + A_E^{-1}) \end{cases} \tag{13}$$

In Equations 9 to 12, the variables have been nondimensionalized by the following scheme:

$$x = \frac{x^*}{h}, \quad z = \frac{z^*}{h}, \quad t = \frac{vt^*}{h^2}\left(\frac{Gr}{A_E^2}\right)^{1/3}$$

$$u = \frac{hu^*}{v(GrA_E)^{1/3}}, \quad w = \frac{hw^*}{v(GrA_E)^{1/3}}$$

$$T = \frac{g\alpha h^3(T^* - T_0)}{v^2(GrA_E)^{2/3}}, \quad F_i^0 = \frac{F_i^{*0}}{F_0}$$

$$\eta_i = \eta_i^* h, \quad p = \frac{h^2 p^*}{\rho_0 v^2}\left(\frac{A_E}{Gr^2}\right)^{1/3} \tag{14}$$

where the starred variables are dimensional. These scales arise

naturally when the velocities are scaled against the energy-limited intrusion velocity.

With this nondimensionalization, the scaling relations (Expressions 6 to 8) reduce to the simple forms

$$t_E \sim A_E^{-4/3} \tag{15}$$

and

$$u_I \sim t^{1/2} \tag{16}$$

$$u_E \sim A_E^{-2/3} \tag{17}$$

The numerical scheme used to solve Equations 9 to 12 is based on the SIMPLE scheme, but defined on a nonstaggered grid. The problems of nonellipticity, resulting in oscillations of the pressure field (which can occur on a nonstaggered grid), were overcome by the use of an elliptic pressure term derived by Armfield (1991), and is fully described there. The discretization is described in Armfield and Patterson (1991); in brief, however, finite volumes are used to convert the derivatives to second-order central differences, with the advective terms approximated by the QUICK scheme of Leonard (1979) and the diffusive terms on the irregular grid by the scheme of Patterson (1983). The time integration is carried out by a second-order Crank–Nicholson predictor corrector method. The discretization produces a block tridiagonal matrix, inverted by an ADI method.

3. Grid tests

In order to resolve the fine scales of the flow near the end walls, near the surface, and in the region of the light–dark boundary, an expanding mesh similar to that used by Armfield (1991) was implemented. The mesh was finest near the end walls, the light–dark boundary, and the upper surface. Since the flow is driven by the radiation absorption in the upper part of the cavity and is influenced strongly by its interaction with the end walls, the lower surface plays only a minor role, and the mesh is not compressed there. The mesh expands away from the walls at constant rates in the horizontal and vertical directions of r_x and r_z from initial values of Δx_1 and Δz_1. In the case of the horizontal mesh, the mesh compresses again after the midpoint of each half of the cavity so that a fine mesh is achieved in the region of the light–dark boundary. To check the dependency of the numerical result on the actual grid, a number of test simulations were performed with the grid parameters shown in Table 1.

Although a number of variables were compared from the different runs, only the isotherms in the shaded region at time $t = 2.92$ are shown in Figure 2. The differences between the runs are typical of those at other times, and of other variables. Clearly, the differences between the various runs is slight in the

Table 1 A summary of the initial dimensionless grid sizes Δx_1 and Δz_1 and the expansion factors r_x and r_z for the grid test runs. The resulting number of mesh points (nodes) is also tabulated

Run	Horizontal grid			Vertical grid			
	Δx_1	r_x	Nodes	Δz_1	r_z	Nodes	Δt
1	0.01	1.05	94	0.001	1.05	82	0.005
2	0.005	1.05	146	0.001	1.05	82	0.005
3	0.01	1.005	182	0.001	1.025	133	0.005
4	0.01	1.05	94	0.001	1.05	82	0.0025

Note: The test simulation used a Grashof number of $Gr = 3.88 \times 10^8$.
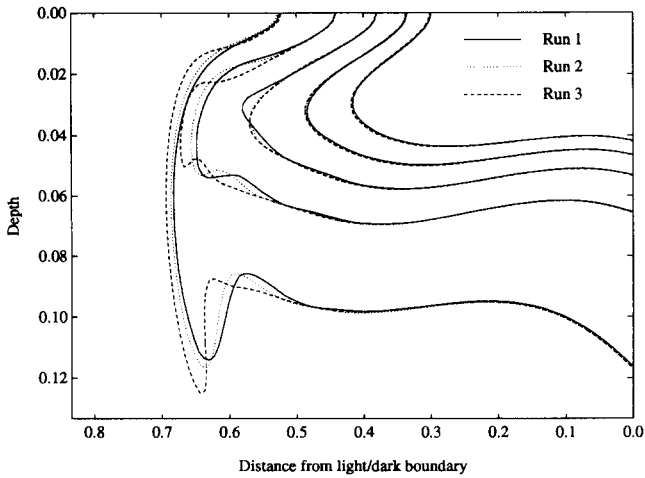
Figure 2 The temperature contours in part of the shaded region for the three runs testing the grid parameters. Run 4 with the finer time interval is not shown, since it was indistinguishable from run 1. The dimensionless temperature contour values are from 1.85 (left or outermost contour) to 9.25 (right or innermost contour) at intervals of 1.85

regions close to the surface and the light–dark boundary, with the maximum deviation occurring in the region where the coarsest grid is located. Run 4, with the shorter time step, is indistinguishable from Run 1 and is not shown. Even so, the error between the coarsest and finest grids is at most only 5%; although this error could be reduced by further reduction in both the initial grid spacing and the expansion factors, doing so was not justified, since the simulations with these grids compare well with the experimental results, as described below. The parameters from run 1 were used in the subsequent numerical experiments.

4. Comparison with experiments

The numerical method was verified by comparison with the three laboratory experiments described in detail in CP. Only one of these is discussed here, since the comparison in all cases was similar. The case considered was for the parameter values $Gr = 4.33 \times 10^8$, $Pr = 7.04$, and $A = A_E = 1$. Using the methods described in CP, the incoming radiation was split into three bands with (nondimensional) intensities of 0.56, 0.34, and 0.21, and attenuation coefficients of 43.5, 4.5, and 0.75, respectively.

The intrusion thickness (d) and the distance it has traveled (l) were measured for both the experiment and the simulation (Table 2). These results are in good agreement, providing one confirmation of the validity of the code.

As another comparison, numerical temperature–time series were compared in Figure 3 with the series obtained from thermistor measurements during three separate but identical runs of the experiment. The thermistors were located at the four (dimensionless) horizontal positions of $x = 0.28, 0.50, 0.72$, and 0.93. Note that the light/dark boundary was located at $x = 1$, so that all thermistors were in the shaded region. The dimensionless depth of the thermistors was 0.07 ($z = 0.93$). The passage of the intrusion is reflected in the lift-off times of the temperature traces, and Figure 3 shows that there is good agreement between the experiments and the numerical simulation. The slope of the temperature–time traces is a reflection of the intrusion velocity, and again, Figure 3 shows that there is good agreement between the two. The divergence

of the numerical temperature–time traces from the experimental traces at approximately $t = 4$ is due to the interaction of the intrusion with the far wall. At this time, the pressure wave begins traveling back along the tank, decelerating the intrusion locally. As the water is temporarily slowed, there is a brief accumulation of hotter water, manifested as a sudden steep rise of the temperature traces. This wave is first seen at the location near the far wall $(x = 0.28)$ and appears progressively later in the locations further from the wall.

While the agreement between experiment and simulation is good, Figure 3 suggests that the numerical velocities are slightly greater than their experimental equivalents. This result is also suggested by the plot of the maximum horizontal velocity at the light/dark boundary against $t^{1/2}$ for both the experiment and the simulation (Figure 4). The faster passage of the simulated intrusion is reflected by the fact that the experimental intrusion takes longer to reach a given velocity than does the simulation, so that the plot of the numerical velocities is shifted to the left to earlier times. However, the important point here is that the data of Figure 4 show that both experiment and simulation have the linear dependence on $t^{1/2}$ expected for the inertial regime from Equation 16.

Table 2 A comparison between the dimensionless intrusion thickness (d) and distance traveled (l) obtained from the experiment and its numerical simulation

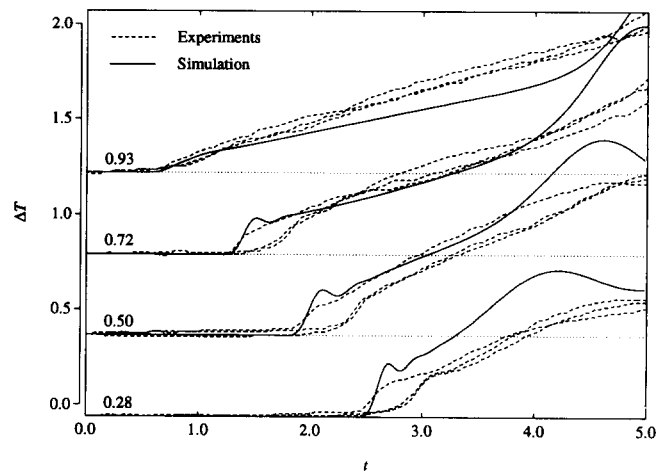|	Experimental		Numerical	
t	d	l	d	l
0.42	0.033		0.050	0.033
0.84	0.100	0.133	0.083	0.117
1.26	0.133	0.267	0.133	0.250
1.68	0.167	0.384	0.167	0.384
2.10	0.200	>0.534	0.217	0.517
2.52			0.250	>0.534

Figure 3 The temperature increases from the thermistor data are compared with a simulated temperature time series. In the experiments, the thermistors were located at a depth of 0.07 ($z = 0.93$) in the shaded region at the four horizontal locations 0.28, 0.50, 0.72, and 0.93. The data from the three repeated runs of the experiment are the dashed lines, while the simulation is the solid line. The traces for each horizontal location are offset from each other, with the corresponding zero temperature (horizontal) axis shown as the dotted line
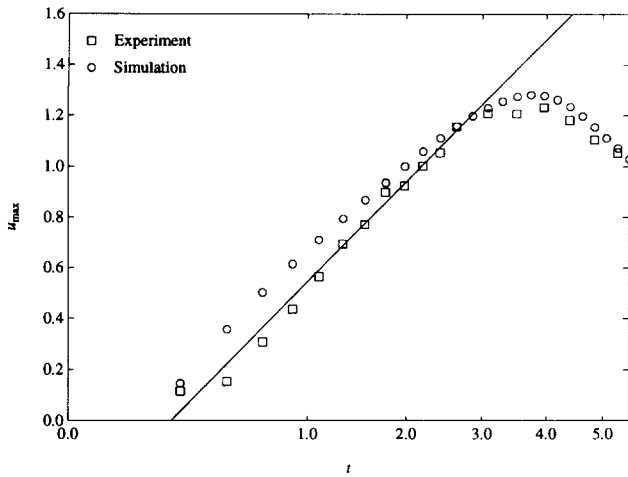
Figure 4 The maximum horizontal velocity at the light/dark boundary plotted as a function of t for the maximum intensity experiment and its simulation. The straight line is the inertial velocity predicted by the scaling

5. Results

One difficulty in generalizing the experimental results is that the intrusion becomes distorted by the interaction with the far wall at approximately the same time as it becomes energy limited (Equation 8). To overcome this limitation, a series of numerical experiments was performed using a shaded region that was twice as long as that of the experiments. In this case, the aspect ratio for the shaded region became $A = h/l = 0.5$, while that of the exposed region remained at $A_E = h/l_E = 1$.

The results from these experiments enabled general (empirical) relations to be determined, allowing the simple determination of the typical velocity and time scales in practical applications. The development of these relations is discussed below.

5.1. Fixed attenuation coefficient

Numerical experiments were performed using a range of values for the Grashof numbers as tabulated in Table 3, with the single value of $\eta = 10$ for the attenuation coefficient. The appropriate velocity with which to characterize the intrusion is the mean velocity, since this is a measure of the volume transferred by the intrusion. Integrating the velocity profile over the dimensionless intrusion depth D gives

$$\frac{V}{Wt} = \int_0^D u(z)dz \tag{18}$$

as the volume V transfer over the time t, where W is the dimensionless width of the intrusion. This is converted to an effective or mean velocity over some vertical length scale δ using $\bar{u} = V/\delta Wt$. The appropriate vertical length scale δ is the bulk radiation scale $1/\eta$ since, in general, the intrusion depth is not known. Thus, Equation 18 becomes

$$\bar{u} = \eta \int_0^D u(z)dz \tag{19}$$

Using Equation 19, the mean inertial velocity was calculated for the numerical experiments, and these have been plotted against $t^{1/2}$ in Figure 5. Here there is a very good fit to the line of the inertial regime, confirming the scaling over four orders of magnitude of Grashof numbers.

Finding the constant of proportionality for Equation 16 for the mean inertial velocity is of importance, since an estimate of the volume V transported during the inertial phase may then be made. The inertial phase may last for some time, as the following example shows. Consider a small pond of depth $h \sim 1$ m and exposed length of $l_E \sim 30$ m, illuminated by solar radiation with an intensity of approximately 600 Wm^{-2}. The Grashof number will be 2.9×10^{11}, and using Equation 8, the flow is expected to become energy limited by $t_E \sim 1500$ s. For a small lake, with $h \sim 3$ m and $l_E \sim 300$ m, this time increases to approximately 6000 s. Consequently, there is a considerable period for which the inertial regime is significant.

The data of Figure 5 show that the early stage of the flow is in good agreement with the inertial regime, with no dependence on the Grashof number, as expected from the scaling analysis. The slope of the line of best fit to the data, as shown in Figure 5, gives the constant of proportionality as 1.03, and in general, the mean inertial velocity can be found from the simple relation

$$\bar{u}_I = 1.03(t^{1/2} - 0.55) \tag{20}$$

The time offset ($t^{1/2} = 0.55$) arises from the fact that a small time t_c, defined by Equation 5, must pass before the flow switches to the inertial-buoyancy balance.

Table 3 The transition times and mean flow velocities for the energy limited regime over a range of Grashof numbers

Gr	t_e	$\bar{u}_e$
10^{11}	3.13	1.05
10^9	3.10	1.00
$10^{8.5}$	3.06	1.00
10^8	3.14	0.98
$10^{7.5}$	—	—

Note: The transition times t_e measured from the numerical results are the times at which the flow velocity becomes constant. The attenuation coefficient was fixed at $\eta = 10$ in these experiments. Energy limited results were not available for the Gr = $10^{7.5}$ experiments.
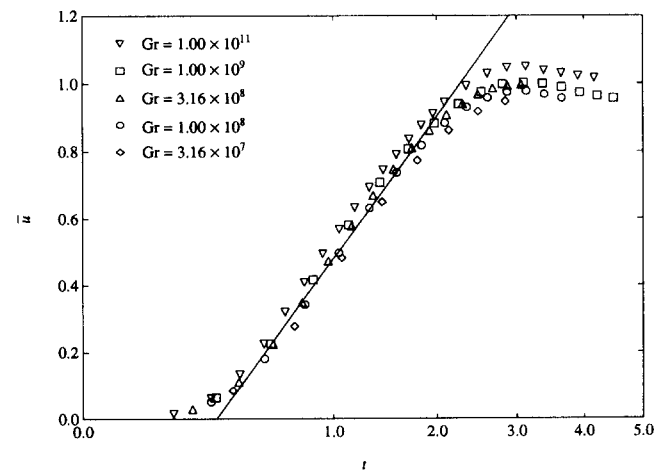

Figure 5 The mean horizontal velocities at the light/dark boundary from the numerical experiments of Table 3 plotted as a function of t. The straight line is the least squares fit to the inertial velocity

At the transition time t_E, the flow velocities should scale as the energy-limited velocity scale (Equation 17). Since Equation 17 is independent of time, the flow velocities should remain constant in time until other balances become important. The data of Figure 5, however, show that this is not the case, in that the observed velocity decreases in time once the flow becomes energy limited. This finding is due in part to the fact that the intrusion continues to thicken, proportional to $\sqrt{vt}$, as it entrains the fluid below. However, the volume transfer must remain constant once the energy-limited flow is reached; otherwise, more energy will be transferred out with the larger volume than the energy entering. This will decrease the forcing term, reducing the velocity until the flow is again in balance. Thus, as the intrusion continues to thicken as a function of $t^{1/2}$, its velocity must decrease at the same rate to keep the volume transfer constant. While the velocity data of Figure 5, for times greater than that at which the peak velocity occurs, are not conclusive, they are consistent with a linear decrease with respect to $t^{1/2}$. Consequently, we will take the maximum value of the data of Figure 5 as representative of the energy-limited velocity for each experiment, and the time at which the maximum value is attained will be used as the transition time.

These measured transition times t_e and velocities $\overline{u_e}$, summarized in Table 3, allow the constants of proportionality for Equations 15 and 17 to be determined. The t_e data indicate that, in general,

$$t_E = 3.1A_E^{-4/3} \tag{21}$$

for the dimensionless energy limited time scale, with a regression coefficient of $r^2 = 1.000$. However, the $\overline{u_e}$ data show that the mean velocity retains a weak dependence on the Grashof number, which is perhaps not unexpected, since the scaling assumes a uniform steplike absorption of radiation with depth, whereas in fact there is a sharp dependence with the greatest absorption near the surface. A least squares analysis yields the relation

$$\overline{u_E} = (0.80 + 0.02 \log_{10} Gr)A_E^{-2/3} \tag{22}$$

for the dimensionless energy-limited mean velocity, with a regression coefficient of $r^2 = 1.000$. However, because the dependence on Gr is weak, a simpler expression can be used for the mean velocity over the range $10^8 \le Gr \le 10^{12}$ with only a small error. This expression is

$$\overline{u_E} = A_E^{-2/3} \tag{23}$$

These relations allow a simple determination of the time to the

Table 4 The dimensionless transition times and flow velocities for the energy-limited regime over a range of dimensionless attenuation coefficients

Run	η_i	η	t_e	$\overline{u_e}$
A	31.6	31.6	3.10	1.07
B	10	10	3.10	1.00
C	5.62	5.62	3.38	0.90
D	3.16	3.16	3.38	0.70
E	31.6, 10	11.7	3.38	0.93
F	10, 3.16	5.0	4.22	0.88
G	100, 31.6, 10	13.2	4.22	0.91
H	31.6, 10, 3.16	6.5	4.50	0.99

Note: The run codes identify the different numerical runs in Figure 6. The fixed Grashof number for these experiments was 10^9, while the effective attenuation coefficient η for each run is tabulated. The attenuation coefficients η_i for the multiple band experiments (E → H) are separated by commas.
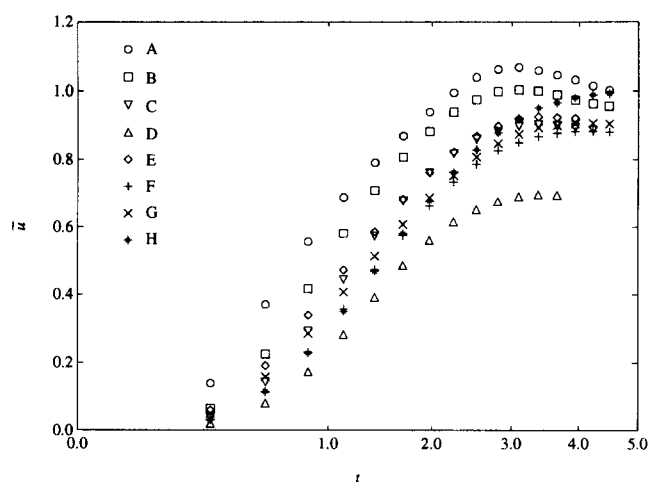
Figure 6 The mean horizontal velocity at the light/dark boundary plotted against t for the experiments of Table 4. The run codes are those of Table 4

onset of the energy-limited regime, and the mean velocity within that regime over a range of Grashof numbers.

5.2. Fixed Grashof numbers

A second series of numerical experiments was performed to determine any further dependence on the attenuation coefficient beyond that predicted by the scaling. These experiments used a fixed value for the Grashof number of 10^9 and covered a range of attenuation coefficients, including several multiple-band models. The effective or bulk values of the attenuation coefficients in these multiple-band experiments were obtained as outlined in CP. For the purposes of the experiments, the models had equal proportions of energy in each of the bands (50% in each of the two-band and 33% in each of the three-band models).

The range of dimensionless attenuation coefficients η_i used in the experiments is shown in Table 4, along with the bulk value η. The mean velocity data at the light/dark boundary for the numerical experiments are plotted against $t^{1/2}$ in Figure 6.

Figure 6 appears to show that the departure from a common slope is more pronounced for the experiments with a varying attenuation coefficient. However, a closer study of Figure 6 indicates that the slopes are in fact similar, with the value of 1.03 obtained earlier, and that it is the onset time t_c of the inertial regime that varies. The variation is due in part to the fact that the radiation is preferentially absorbed in the surface layers, forming the hot boundary layer discussed in the previous section. Since this layer is only very slowly moving, heat is not being advected away at the rate expected by the scaling, and the transition is delayed.

An estimate of the onset time can be obtained by plotting the measured transition time t_c to the inertial phase against the attenuation coefficient (Figure 7). A least squares analysis yields

$$t_c = 0.81 - 0.42 \log_{10} \eta \tag{24}$$

and the mean velocity in general would become

$$\overline{u_I} = 1.03(t^{1/2} - t_c^{1/2}) \tag{25}$$

The energy-limited time and velocity scales were obtained from Figure 6 as described above (section 5.1) and have been tabulated in Table 4. They also show a dependence on the attenuation coefficient beyond that predicted by the scaling. To facilitate the development of a general equation, we will remove
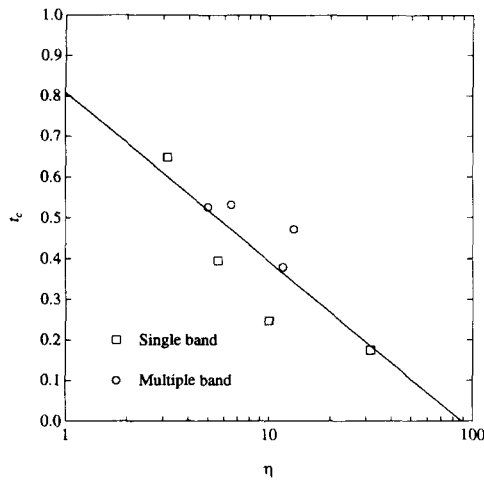
Figure 7 The transition time to the inertial regime t_c plotted against the attenuation coefficient η for the experiments of Table 4

velocities that will occur beneath such mats. We consider a small pond typical of swampy areas having a depth of 1 m and partially covered with a plant layer. We will assume that an area of open water remains, so that the exposed length is 10 m. Thus $h = 1$ m and $l_E = 10$ m, so that $A_E = 0.1$.

We let the incoming radiation have a maximum surface intensity of $F_0 = 1000$ Wm^{-2} at midday, typical for a cloudless summer day in southern Australia (Coates and Ferris 1994), and we let the average attenuation coefficient be 2.0 m^{-1}, equivalent to assuming that the pond bottom is just visible. Using these values, the Grashof number is 4.7×10^{11} and the dimensionless attenuation coefficient is 2.0.

With these parameters, the flow will become energy limited after a (nondimensional) time of $t_E = 67$ from Equation 21, and the energy-limited velocity from Equation 29 is found to be $u_E = 2.7$. These correspond to a real time of 0.5 hours and a real velocity of 10 mms^{-1} using the conversions in Equations 14. This velocity is relatively large, and indicates that over a 12-hour day at maximum velocity, a typical intrusion in the small pond would travel up to 430 meters, carrying nutrients to the plants over a large area.
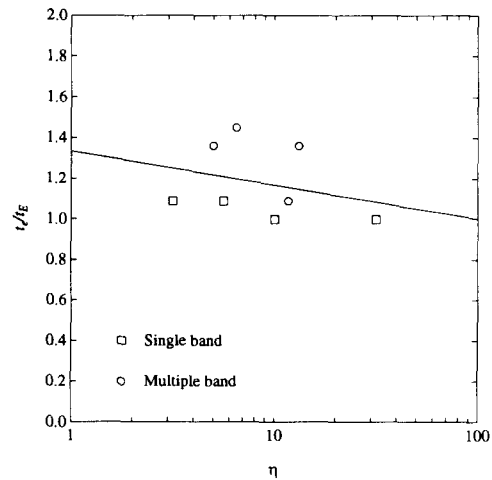
the Grashof number dependence by scaling the values from Table 4 with the values expected at Gr = 10^9, obtained from Equations 21 and 22.

A semilogarithmic plot of the scaled transition times t_e/t_E against the attenuation coefficient (Figure 8) shows a linear trend for the single band attenuation coefficient experiments of Table 4. The agreement is not as good when the multiple attenuation experiments are included, since the scaling cannot predict the interaction of the individual bands. Nevertheless, the use of a single relation enables a reasonable estimate of the transition time to be made under a variety of conditions, and as such, it is worth developing such a relation. A least squares fit to the data of Figure 8 gives the relation

$$\frac{t_e}{t_E} = 1.33 - 0.17 \log_{10} \eta \tag{26}$$

or

$$t_e = (4.14 - 0.53 \log_{10} \eta)A_E^{-4/3} \tag{27}$$

using the earlier result of $t_E = 3.11$ (Equation 21).

Similarly, a semilogarithmic plot of the scaled mean energy-limited velocity $\bar{u}/\bar{u}_E$ against the attenuation coefficient (Figure 9) shows a good agreement to a linear trend for all the experiments of Table 4. From these experiments, the mean energy-limited velocity is, in general,

$$\frac{\bar{u}}{\bar{u}_E} = 0.33 + 0.79 \log_{10} \eta \tag{28}$$

or

$$\bar{u} = (0.33 + 0.79 \log_{10} \eta)(0.80 + 0.02 \log_{10} \text{Gr})A_E^{-2/3} \tag{29}$$

using Equation 22 for $\bar{u}_E$. Alternatively, over the range $10^8 \le \text{Gr} \le 10^{12}$, the simpler expression

$$\bar{u} = (0.33 + 0.79 \log_{10} \eta)A_E^{-2/3} \tag{30}$$

can be used.

6. An example

As discussed in section 1, the presence of floating vegetation mats can act as an opaque layer on the water surface. The equations developed above enable us to estimate the typical

Figure 8 The transition times are plotted against $\log_{10} \eta$ for the numerical simulations for the energy-limited regime. The times have been scaled against t_E
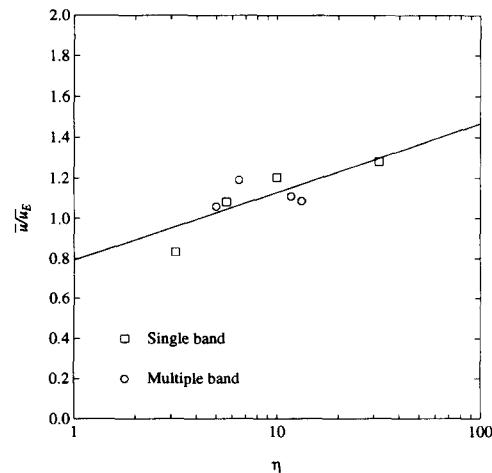

Figure 9 The mean velocities are plotted against $\log_{10} \eta$ for the numerical simulations for the energy-limited regime. The velocities have been scaled against $\bar{u}_E$

This estimate is an upper limit because the calculation assumes that the plants form a completely opaque layer, whereas in fact the plant layer is likely to allow some transmission of radiation, with a corresponding reduction in the temperature differential between the shaded and unshaded water. The flow velocity will also be smaller during the early part of the day, since the surface intensity and through it the Grashof number vary throughout the day. In this example, the onset of the energy-limited regime was calculated using the midday maximum intensity, while the result indicated that the onset time is only a half hour after dawn. Reducing the flux will increase the onset time and decrease the velocity. Even assuming that these factors reduce the incoming flux to 10% of the maximum value, the energy-limited velocity is only reduced to 50% of its maximum value, since the Grashof number appears as $Gr^{1/3}$ in the nondimensionalizing equations (Equations 14). Consequently, these intrusions could be of importance to the biological dynamics of such ponds.

7. Conclusions

A numerical code based on the SIMPLE algorithm and defined on a nonstaggered grid was used to simulate the natural convection in a cavity that was nonuniformly heated by the absorption of radiation entering through the surface. It was shown that the results from the code agree with the earlier experiments of CP over a range in the radiation parameters. The code was then used to extend that parameter range, and from the results, empirical relations were derived that would enable the intrusion velocities and transition times to be determined in more general cases. The velocities at any particular radiation flux can be determined by Equations 25 and 22, with the transition time between these two scales given by Equation 21. The radiation flux enters these equations via the Grashof number (Equation 1). These velocity and time scales can be corrected for the varying attenuation coefficient, using Equations 24 to 29. From these relations, the volume of water transported by the intrusion can be predicted. A simple example showing the application of these equations is given.

Acknowledgments

References

Armfield, S. W. 1991. Finite-difference solutions of the Navier–Stokes equations on staggered and non-staggered grids. *Comput. Fluids,* **20,** 1–17

Armfield, S. W. and Patterson, J. C. 1991. Direct simulation of wave interactions in unsteady natural convection in a cavity. *Int. J. Heat Mass Trans.,* **34,** 929–940

Coates, M. J. 1991. Differential absorption due to an opaque layer. Ph.D. thesis, Department of Civil and Environmental Engineering, University of Western Australia (Environmental Dynamics Reference ED-578-MC)

Coates, M. J. and Patterson, J. C. 1993. Unsteady natural convection in a cavity with nonuniform absorption of radiation. *J. Fluid Mech.,* **256,** 133–161

Coates, M. J. and Ferris, J. M. 1994. The radiatively driven natural convection beneath a floating plant layer. Environmental Dynamics Reference ED-581-MC, Centre for Water Research, University of Western Australia. *Limn. Ocean,* in press

Kirk, J. T. O. 1986. Optical limnology—a manifesto. In *Limnology in Australia,* P. De Deckkar and W. D. Williams (eds.). CSIRO, Melbourne and Dr W. Junk, Dordrecht, 33–62

Leonard, B. P. 1979. A stable and accurate convective modelling procedure based on quadratic upstream interpolation. *Comp. Meth. Appl. Mech. Eng.,* **19,** 59–98

Patterson, J. C. 1983. General derivative approximations for finite difference schemes. *Int. J. Numer. Meth. Eng.,* **19,** 1235–1241

Patterson, J. C. 1984. Unsteady natural convection in a cavity with internal heating and cooling. *J. Fluid Mech.,* **140,** 135–151

Trevisan, O. V. and Bejan, A. 1986. Convection driven by the nonuniform absorption of thermal radiation at the free surface of a stagnant pool. *Numer. Heat Transfer,* **10,** 483–506